Article

Phase-interface-anchored cadmium single-atom catalysts for efficient methanol steam reforming

Check for updates

Shunan Zhang[1], Haozhi Zhou[1], Zilong Shao[2], Baohuan Wei[3], Zhen Hu[3], Hao Liang[1], Ruonan Zhang[1], Xiaofang Liu[2], Hu Luo[2], Lin Xia[2], Yuhan Sun [1,3] & Hui Wang [1,2] ✉

Employing interface engineering to design innovative single-atom catalysts (SACs) for effective methanol steam reforming (MSR) presents an attractive yet formidable challenge. Here, we report phase-interface confined Cd/P25 SACs, where Cd atoms are stably anchored at the phase interface between anatase (101) and rutile (110) facets. The Cd-O-Ti phase interface sites formed exhibit asymmetric geometric and electronic properties that enable 100% methanol conversion, a low CO concentration (~0.1 mol%) in the effluent gas, and sustained stability exceeding 150 h. The H_2 production rate at these interface sites is approximately 15-fold and 8-fold higher than that of anatase and rutile surface sites, respectively. Enhancing the phase interface density through atmosphere pretreatment can further increase the H_2 production rate by an additional 11%. Furthermore, these powder SACs can be 3D printed into kilogram-scale monolithic catalysts, advancing practical in-situ hydrogen generation applications.

Methanol steam reforming (MSR), a pivotal and cost-effective technology for on-site hydrogen generation, when integrated with polymer electrolyte membrane fuel cells (PEMFCs), has markedly advanced the trajectory of hydrogen energy systems towards decentralization, miniaturization, and portability, particularly in the transportation sector[1]. Conventional Cu-based and noble metal-based nanoparticle catalysts are often plagued by limited stability and high CO selectivity[2–5], leading to shortened operational lifespans and Pt electrode poisoning in integrated PEMFCs. This challenge arises from the ambiguity surrounding the surface atomic active sites within nanoparticle catalysts, which hampers the precise tuning of microstructural and local electronic properties.

Single-atom catalysts (SACs), with their distinct ability to finely modulate atomic-scale structures and local electronic properties beyond the reach of nanoparticle catalysts, have been the focus of intensive research aimed at the targeted enhancement of catalytic performance across a spectrum of reactions[6,7]. The presence of abundant defects within the support is essential for the formation of stable SACs, with the local coordination environment of these defects playing a decisive role in shaping the properties and reactivity of the single atoms[8,9]. Employing interface engineering in support materials is an effective approach to regulating the defect properties. This is because interfaces, such as twin boundaries, phase interfaces, and heterojunctions, which are defect-rich regions, typically exhibit enhanced polar electronic domains and unique coordination geometries, resulting in a substantial increase in catalytic activity[10–15]. However, modulating and utilizing interface-specific structures to precisely confine and anchor single atoms has not been previously reported and remains a formidable challenge, primarily attributed to complex interfacial structures and the energy mismatch associated with traditional metals. The influence of the interface microenvironment on the properties of single atoms and their reactivity is not yet fully understood, presenting a critical gap in the development of highly efficient SACs.

[1]Institute of Carbon Neutrality, ShanghaiTech University, Shanghai, PR China. [2]CAS Key Laboratory of Low-Carbon Conversion Science and Engineering, Shanghai Advanced Research Institute, Chinese Academy of Sciences, Shanghai, PR China. [3]Shanghai Institute of Clean Technology, Shanghai, PR China. ✉e-mail: wanghh@sari.ac.cn

Reducible TiO_2, widely recognized as an ideal and specific support, has garnered substantial research attention, with a particular focus on P25 and its phase interfaces[16–19]. Cutting-edge studies have identified that the interfaces between anatase and rutile could act as conduits for significantly enhancing electron transfer, leading to robust activation and dissociation of H_2O in photocatalysis[20–23]. Building on this insight, seeking and anchoring single atoms as active sites for CH_3OH dissociation at these phase interfaces to create cooperative catalytic sites may constitute an effective strategy for designing highly efficient MSR catalysts.

Herein, we successfully fabricate the phase-interface-confined Cd/P25 SACs. The stable anchoring of Cd atoms at the anatase (101)-rutile (110) phase interface is facilitated by their energetic compatibility and the presence of abundant interfacial Ti defects. Various characterizations reveal that these unique Cd–O–Ti phase interface cooperative sites confer high activity and stability in the MSR reaction. The H_2 production rate at these phase interface sites is approximately 15-fold and 8-fold higher than that of anatase and rutile surface sites, respectively. By tuning the phase interface density, we achieve an enhanced H_2 production rate of 292.9 mmol $g_{cat}^{-1} h^{-1}$. Additionally, the reaction energy barrier for the formate decomposition pathway is significantly lowered at these phase interface sites, leading to CO selectivity (C mol%) below 0.5%. Notably, such SACs can be 3D printed into monolithic catalysts at the kilogram scale, markedly advancing their technological viability and practical application prospects.

Results

Catalytic performance of TiO_2-supported catalysts in MSR

To initially explore the effects of P25 properties on active metals in the MSR reaction, we systematically incorporated 5 wt% of Cu, Pd, Pt, and Cd onto Degussa P25 using a vacuum rotary impregnation technique. The Cd-incorporated P25 catalyst (5Cd/P25) exhibited exceptional performance under reaction conditions (290 °C, 0.1 MPa; steam-to-carbon (S/C) ratio = 3/1; N_2 carrier gas flow = 30 mL min^{-1}; liquid feed rate = 3 mL $g^{-1} h^{-1}$): achieving complete methanol conversion (100%) while maintaining ultralow CO concentration (0.13 mol%) in the effluent gas and CO selectivity below 0.5% (Fig. 1a). This performance stood in stark contrast to the traditional MSR-active metals Cu, Pd, and Pt, which, when supported on P25, failed to achieve full conversion and exhibited a CO selectivity greater than 2%. Moreover, when Cd was deposited on alternative supports such as SiO_2, ZnO, CeO_2, and ZrO_2, the CH_3OH conversion was lower than 10%. These findings underscore the distinctive catalytic properties conferred by the interaction between Cd and the P25 support. We further evaluated the influence of the crystalline phase of TiO_2 on the performance of Cd-supported catalysts. Upon examining 5Cd/A (anatase) and 5Cd/R (rutile), and their mixture (composed of 80% 5Cd/R and 20% 5Cd/A), we observed CH_3OH conversions of 21.0%, 39.0%, and 18.1% at 290 °C, respectively (Fig. 1b and Supplementary Fig. 1). These corresponded to CO selectivity of 3.6%, 2.2%, and 3.7%, respectively. In stark contrast, the H_2 production rate for 5Cd/P25 soared to 97.7 mmol $g_{cat}^{-1} h^{-1}$, outperforming the rates for 5Cd/A, 5Cd/R, and their mixture by factors of 4.9, 2.6, and 5.6, respectively. Additionally, adjusting the mixture ratio still failed to achieve reaction performance comparable to that of 5Cd/P25 (Supplementary Fig. 2), underscoring the unique catalytic properties of this catalyst. Notably, Cd-containing catalysts do not require H_2 reduction prior to the reaction, a step traditionally necessitated by Cu-based or noble metal catalysts (Supplementary Fig. 3). This eliminates the need for pre-reduction, simplifying the reforming apparatus and reducing operational costs. Moreover, it enhances the catalysts' compatibility with the dynamic start-stop cycles of PEMFCs, thereby facilitating more efficient energy management.

Our study revealed an initial increase followed by a decrease in both CH_3OH conversion and H_2 production rate as the Cd content varied from 1 to 10 wt% on P25, with optimal performance at the 5 wt%

loading (Supplementary Fig. 4). The Cd-based catalysts exhibited enhanced operational stability (Supplementary Fig. 5), with 5Cd/P25 demonstrating exceptional durability by maintaining a stable H_2 production rate (>97.0 mmol $g_{cat}^{-1} h^{-1}$) and CO selectivity below 0.5% throughout a rigorous 150 h continuous test (Fig. 1c). The 5Cd/P25 catalyst displayed the lowest apparent activation energy, measured at 107.3 ± 0.6 kJ mol^{-1}, significantly outperforming its counterparts: 5Cd/A with an apparent activation energy of 146.6 ± 0.5 kJ mol^{-1}, and 5Cd/R at 121.9 ± 0.6 kJ mol^{-1} (Fig. 1d and Supplementary Fig. 6). This lower energy barrier was a key factor contributing to the superior catalytic performance of the 5Cd/P25 in the MSR process. Our optimization endeavors with the 5Cd/P25 catalyst yielded a H_2 production rate of 158.4 mmol $g_{cat}^{-1} h^{-1}$, with complete CH_3OH conversion of 100% and a minimal CO selectivity of 0.4%, realized by elevating the S/C ratio to 1/1 (Supplementary Fig. 7). However, an excess S/C ratio beyond 1/1 led to a decline in CH_3OH conversion and the emergence of CH_4, likely due to competitive adsorption of reactants on the catalyst surface. At the optimal S/C ratio of 1/1, reducing the feed rate from 3 to 0.5 mL $g^{-1} h^{-1}$ enabled complete CH_3OH conversion (100%) even at a reduced temperature of 250 °C (Supplementary Fig. 8). The maximum H_2 production rate achieved was 267.9 mmol $g_{cat}^{-1} h^{-1}$ at a rate of 6 mL $g^{-1} h^{-1}$, which was 14.7-fold and 7.7-fold higher than the rates of 5Cd/A and 5Cd/R, respectively, under identical conditions (Supplementary Fig. 9). The hydrogen-production activity of the system meets the state-of-the-art requirements for PEMFC vehicle applications (see "Methods" section).

Uncovering the geometric and electronic properties of active sites

To elucidate the disparities in catalytic performance influenced by the crystalline phase, we conducted an in-depth comparative analysis of the micro-geometric and electronic properties. The inductively coupled plasma optical emission spectrometry (ICP-OES) analysis revealed similar actual Cd loadings in the 5Cd/A (4.6 wt%), 5Cd/R (4.8 wt%), and 5Cd/P25 (4.9 wt%) catalysts. X-ray diffraction (XRD) patterns revealed the absence of diffraction peaks for Cd species in both 5Cd/P25 and 5Cd/A, indicative of their well-dispersed state (Fig. 1e). Conversely, the presence of $CdTiO_3$ species on 5Cd/R was corroborated by XRD and Raman spectroscopy (Supplementary Fig. 10). Calculations showed a significantly lower lattice mismatch of 2.4% between CdO and R, in contrast to the 24.1% mismatch with A (Supplementary Table 1). This smaller mismatch likely facilitated the formation of $CdTiO_3$ on R. X-ray photoelectron spectroscopy (XPS) and Auger electron spectroscopy (AES) confirmed the oxidation states of Cd species as +2, with no metallic Cd detected (Fig. 1f and Supplementary Fig. 11). X-ray absorption near-edge spectroscopy (XANES) provided corroborating evidence that the white line features of all examined samples closely resembled those of the CdO reference (Fig. 1g). Extended X-ray absorption fine structure (EXAFS) analysis revealed the presence of only Cd–O scattering paths at approximately 2.24 Å in all samples, with coordination numbers of 6.2, 5.4, and 5.8 for 5Cd/A, 5Cd/R, and 5Cd/P25, respectively (Fig. 1h and Supplementary Table 2). These findings suggest that Cd exists as isolated atoms in the three catalysts, exhibiting a coordination geometry similar to that of the surface Ti atoms, characterized by octahedral or square pyramidal structural motifs. To further reveal the atom configuration, we employed transmission electron microscopy (TEM) analysis. The average particle sizes of A, R, and P25 were 21.5, 44.0, and 29.5 nm, respectively, with no evidence of Cd species particles (Supplementary Fig. 12). Energy-dispersive X-ray spectroscopy (EDS) mapping images showed the high dispersion of Cd species on the surface of A and R (Fig. 1i, j), while most Cd species were predominantly situated at the interface between P25 particles (Fig. 1k). High-angle annular dark field scanning transmission electron microscopy (HAADF-STEM) further revealed atomically dispersed Cd atoms (bright contrast spots) on A (101) and R (110) facets of 5Cd/A and 5Cd/R
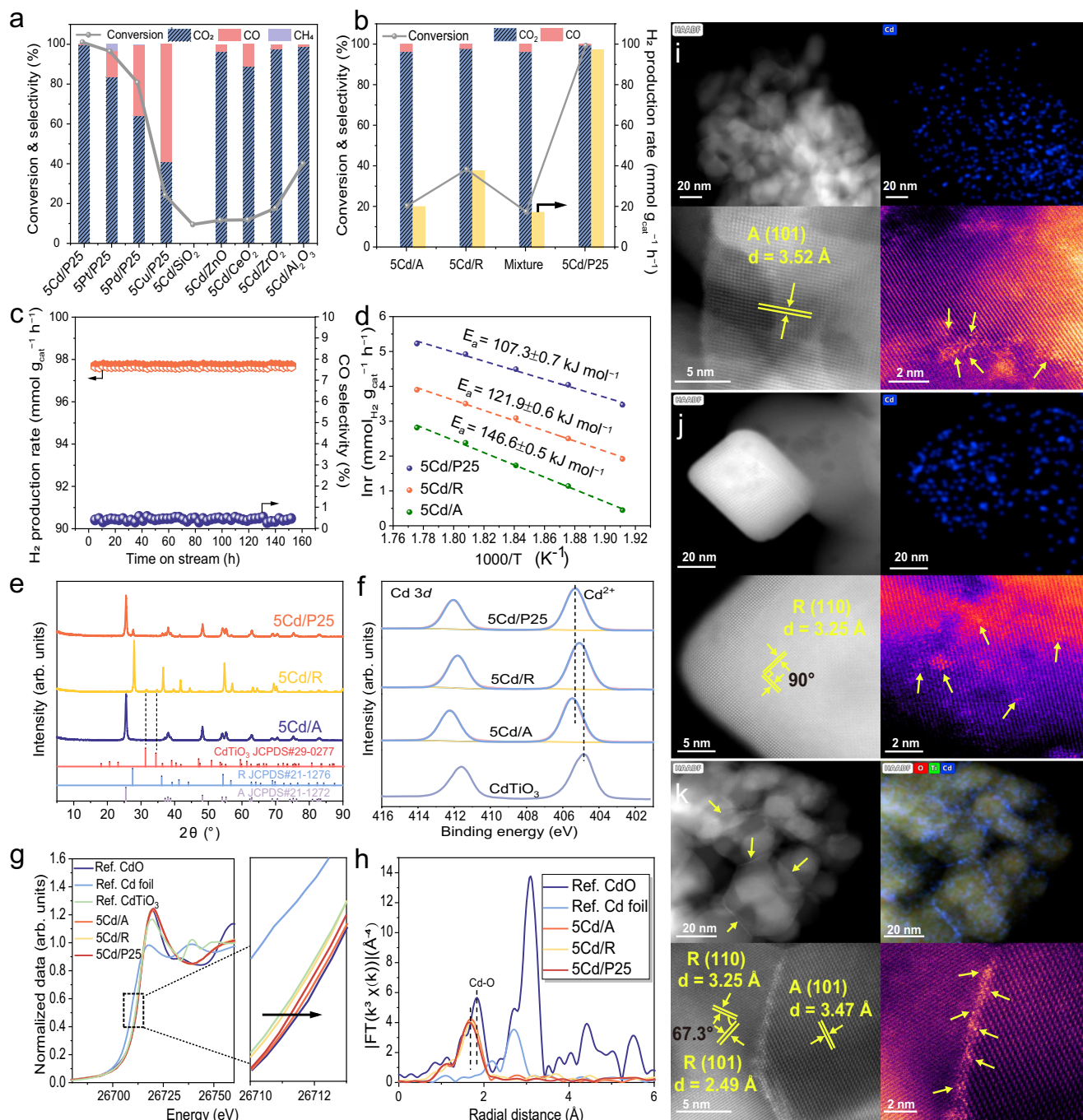
Fig. 1 | Catalytic performance and structural characteristics of catalysts in the MSR reaction. a, b Methanol conversion, product selectivity, and H_2 production rate for various catalysts. **c** Long-term stability test of 5Cd/P25. Reaction conditions: 290 °C, S/C molar ratio = 3/1, 0.1 MPa, N_2 carrier gas flow = 30 mL min^{-1}, liquid feed rate = 3 mL g^{-1} h^{-1}. **d** Apparent activation energy evaluation (methanol conversion less than 10%). **e** XRD patterns of fresh catalysts. **f** XPS spectra of the Cd 3d orbitals for fresh catalysts. **g** Cd K-edge XANES spectra of fresh catalysts. **h** K^3-weighted χ (k) function of EXAFS spectra. HAADF-STEM and EDS elemental maps for 5Cd/A (**i**), 5Cd/R (**j**), and 5Cd/P25 (**k**) catalysts (isolated Cd atoms highlighted by a yellow arrow).

(Supplementary Figs. 13 and 14). Notably, in the 5Cd/P25 catalyst, Cd single atoms were primarily anchored at the anatase (101)/rutile (110) phase interface, as evidenced by the distinct bright contrast band observed along the interfacial boundary in Fig. 1k and Supplementary Fig. 15. Moreover, bright contrast spots were observed along the Ti atomic rows, implying that in all three samples, Cd may be situated at surface Ti defects and bonded with lattice oxygen to form SACs characterized by a Cd−O−Ti configuration. Based on the above results, models of Cd$_1$/A (101), Cd$_1$/R (110), and Cd$_1$/A (101)-R (110) were constructed using density functional theory (DFT) calculations,

corresponding to the 5Cd/R, and 5Cd/P25 catalysts, respectively (Supplementary Fig. 16). The coordination structure of the interface Cd−O−Ti site exhibited asymmetry, which was markedly distinct from the symmetric structure of the surface site. Therefore, it could be inferred that the variation in performance was attributable to subtle differences in the coordination environment of the single atoms, which underscored the distinctive coordination of the Cd atom at the P25 phase interface.

To identify the actual active sites and their configurations during the reaction, an in-depth analysis of the spent catalysts was conducted.

Post-reaction examination revealed subtle peaks indicative of CdTiO$_3$ in the XRD patterns of the 5Cd/P25 catalyst (Supplementary Fig. 17). This observation suggests that the formation of CdTiO$_3$ may have originated from the transformation of a limited number of isolated Cd atoms present on the R phase of P25, as no such transformation was detected in the 5Cd/A catalyst. The oxidation state of Cd in all spent SACs remained around +2, as confirmed by XPS, XANES, and EXAFS analyses, with no evidence of metallic Cd or CdO (Supplementary Figs. 18 and 19). By contrast, the Cd-O coordination numbers for the 5 Cd/R exhibited a significant increase from 5.2 to 6.2 (Supplementary Table 3), likely due to the partial transformation of Cd single atoms into CdTiO$_3$. This finding could account for the initial drop in CH$_3$OH conversion from ~40% to ~25% (Supplementary Fig. 5b). Similarly, a decline in CH$_3$OH conversion was noted, concurrently with the pronounced emergence of CdTiO$_3$, when the loading of Cd surpassed 5 wt % in the 5Cd/P25 catalyst (Supplementary Figs. 4 and 20). Moreover, the synthesized CdTiO$_3$ and CdTiO$_3$/TiO$_2$ demonstrated negligible catalytic activity under identical reaction conditions, effectively ruling out CdTiO$_3$ as an active species (Supplementary Table 4).

The structure and reaction performance of the 5 Cd/P25 catalyst were unaffected by H$_2$ reduction at 290 °C (Supplementary Figs. 3 and 21). However, when the reduction temperature was increased to 400 °C, a sharp decrease in CH$_3$OH conversion from 100% to 33.6% was observed (Supplementary Fig. 22). HAADF-STEM revealed the formation of sub-nanometer Cd clusters, corroborated by EXAFS spectra showing prominent Cd-Cd coordination at ~2.8 Å, suggesting that metallic Cd or clusters were detrimental to catalytic activity (Supplementary Fig. 23). Additionally, the absence of CH$_3$OH conversion over pure metallic Cd and CdO supported the conclusion that Cd single atoms were the exclusive active species (Supplementary Table 4). Cd species supported on alternative oxides like ZrO$_2$, although achieving atomic dispersion, exhibited inferior catalytic performance (Fig. 1a and Supplementary Fig. 24). This suggests that the Cd-O-Ti configuration is a more effective active site, particularly

at phase interfaces. The H$_2$ production rate was normalized against the specific surface area of TiO$_2$ (Supplementary Table 5) to assess the intrinsic catalytic activity. Despite this normalization, the 5Cd/P25 catalyst, with a smaller specific surface area, showed the highest H$_2$ yield (2.2 mmol m^2 h^{-1}). This indicates that the superior catalytic performance is independent of the textural properties of TiO$_2$ (Supplementary Fig. 25). In situ electron paramagnetic resonance (EPR) measurements disclosed that the 5Cd/P25 catalyst displayed the weakest oxygen vacancy signal under reaction conditions (Fig. 2a). Moreover, quasi-in situ XPS experiments showed that the oxygen vacancy concentration remained relatively stable (10-12% area ratio) with negligible impact on the oxidation state or electronic properties of Cd species (Supplementary Fig. 26). Consequently, the results ruled out the hypothesis that oxygen vacancies played a dominant role in dictating the reaction activity, while highlighting that the exceptional performance originated from the Cd-O-Ti interfacial sites.

The electronic properties of the Cd-O-Ti sites on three SACs were further investigated. The binding energy of the Cd 3$d_{5/2}$ peak for 5Cd/P25 was measured at 405.3 eV, which was intermediate between the values for 5Cd/A (405.5 eV) and 5 Cd/R (405.1 eV) (Fig. 1f). Intriguingly, the white line energies followed a similar trend, with the estimated oxidation states of Cd being +1.87, +1.75, and +1.63 for 5Cd/A, 5Cd/P25, and 5Cd/R, respectively, derived from the 0.5 position of the normalized near-edge intensity (Fig. 2b). The correlation between the oxidation states and coordination numbers, similar to the Sabatier principle, elucidated the unique electronic properties conferred by the Cd-O-Ti interface sites. Electron energy loss spectroscopy (EELS) showed a shift of the Ti L-edge to lower energies upon anchoring Cd single atoms at the phase interface of P25, confirming electron transfer from Cd to Ti atoms and the consequent formation of a strong interaction (Fig. 2c). This finding was corroborated by H$_2$-TPR experiments, which recorded a higher reduction temperature for the 5Cd/P25 catalyst, indicative of the enhanced stability and interaction at the Cd-O-Ti interface sites (Supplementary Fig. 27). Electrochemical cyclic voltammetry (CV)
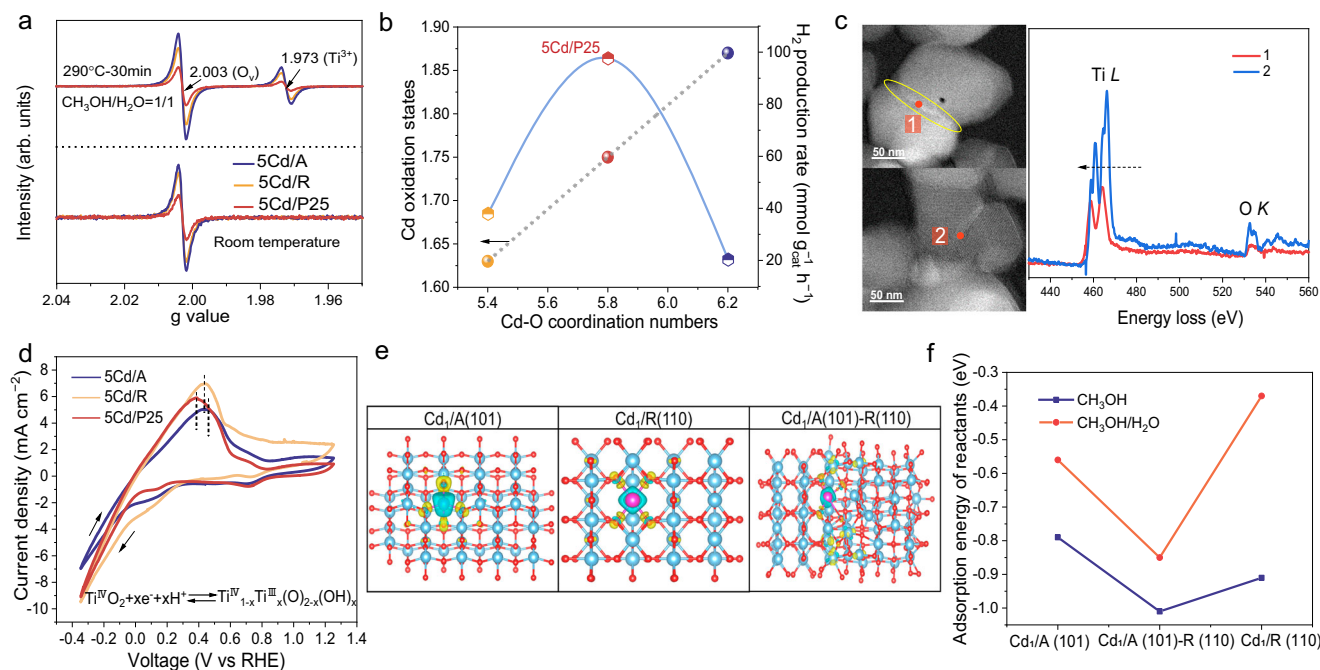

Fig. 2 | Electronic properties of actual active sites. a In situ EPR spectra at a S/C molar ratio of 1/1 under ambient and 290 °C conditions. **b** Sabatier-type correlations between Cd-O coordination number, Cd oxidation state, and H$_2$ production rate. **c** Atomic-resolution HAADF-STEM with Ti L-edge EELS spectra across anatase/rutile interface. **d** Electrochemical CV curves in 0.1 M H$_2$SO$_4$ solution. **e** Charge density differences of structure models (Ti atoms: light blue; O atoms: red; Cd atoms: purple). Yellow and green indicate the gain and loss of electrons, respectively. **f** DFT-calculated adsorption energies for CH$_3$OH and co-adsorbed CH$_3$OH/H$_2$O on Cd$_1$/A (101), Cd$_1$/R (110), and Cd$_1$/A (101)-R (110).

indirectly assessed the electron transfer capability, with the 5Cd/P25 catalyst exhibiting a lower oxidation peak voltage—corresponding to the electron release process as depicted in Fig. 2d—compared to other catalysts[24]. This finding suggests a more rapid electron transfer rate, which is likely to enhance the adsorption and activation of reactants. Furthermore, due to its asymmetric structure, the interface showed an asymmetric charge density (polar electronic domain) in the charge density difference distribution analysis (Fig. 2e), and exhibited a higher electron density of state (Supplementary Fig. 28). This enhanced electron state density enabled the interfacial Cd atom to have the lowest reactant adsorption energy (Fig. 2f). The stronger adsorption and activation capabilities for reactants were verified through the temperature-programed desorption (TPD) experiments of CH_3OH (Supplementary Fig. 29). In general, the distinctive and asymmetric geometric and electronic properties of the Cd–O–Ti sites at the phase interface are instrumental in elucidating the enhanced catalytic performance observed in the 5Cd/P25 catalyst.

Phase interface sites formation, modulation, and impact

To disclose the structural specificity underlying the anchoring of Cd single atoms at the interface between A (101) and R (110), surface defects of the supports were investigated using positron annihilation lifetime spectra (PALS, Supplementary Fig. 30 and Supplementary Table 6). The lifetime components τ_1 and τ_2 were assigned to positrons captured by monovacancies and larger defect clusters, respectively[25,26]. In contrast, the P25 support exhibited a shorter lifetime τ_2 (364 ps), alongside the highest relative intensity (I_2), which might have been attributed to a high concentration of defect clusters. DFT calculations revealed that the formation energy of Ti vacancy defects at the phase interface was significantly lower than within the bulk phase surface, indicating a higher likelihood of their formation at these interfaces (Supplementary Fig. 31). We tentatively inferred that the phase interface of A and R provided abundant defects, such as Ti vacancy clusters, that anchored the Cd single atoms. HAADF-STEM further elucidated the microstructure of the phase interface in pure P25. Lattice discontinuities and irregularities were clearly identified at the interface between the A (101) and R (110) facets, as shown by the gray line in Fig. 3a, indicating the presence of interface defects. Atomic-resolution characterization further revealed that subtle disorder in the interfacial atomic arrangement was confined to a narrow region at the interface, as highlighted by the white circle in Fig. 3b. These observations were likely due to surface atom rearrangements
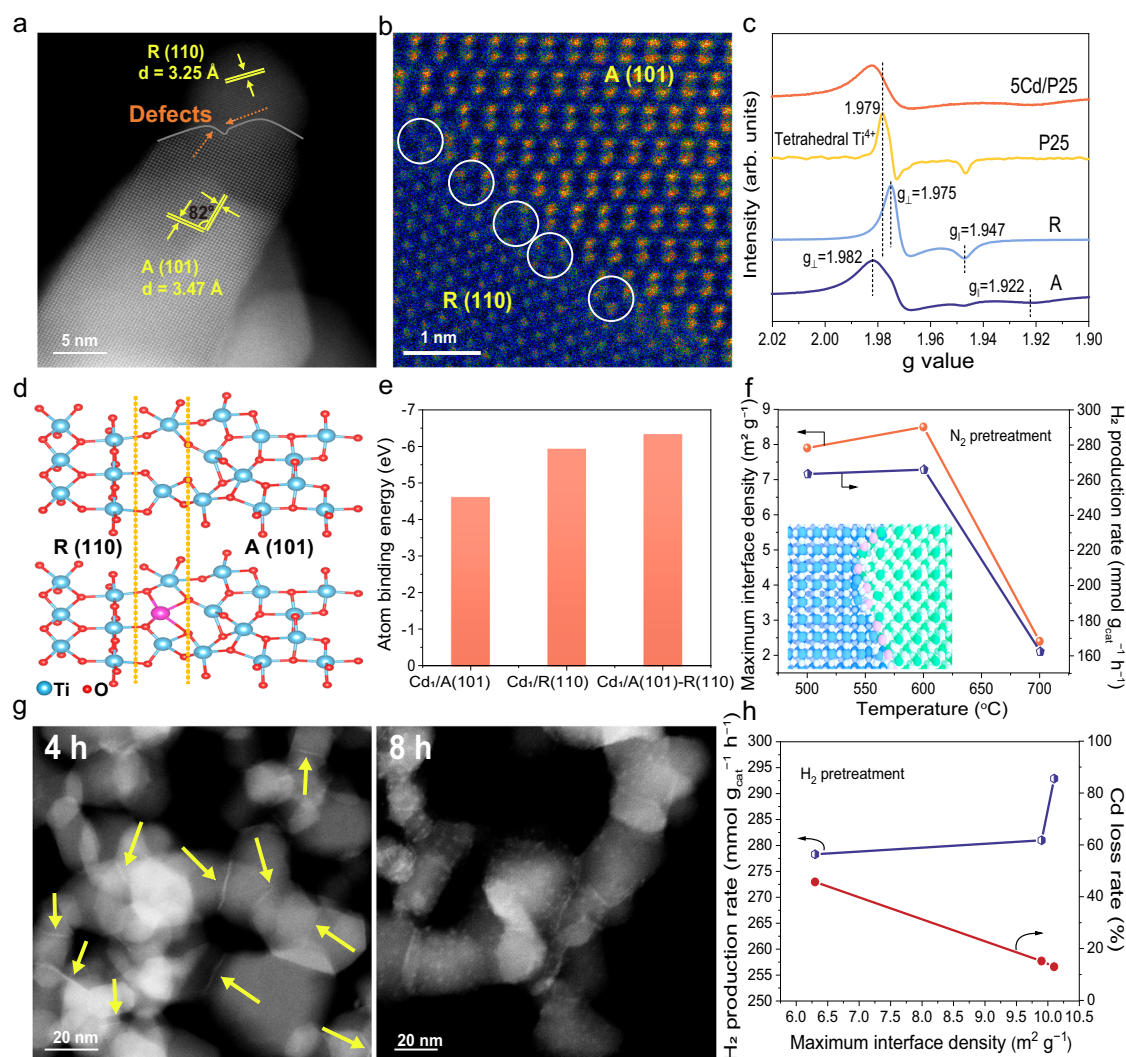

Fig. 3 | Formation and modulation of phase interface sites. a, b HAADF-STEM images of the phase interface in P25. **c** Low-temperature EPR spectra acquired after UV light illumination at 20 °C in the presence of 2, 4, 6-trichlorophenol. **d** Theoretic structure models of A (101)-R (110) (upper) and Cd₁/A (101)-R (110) interfaces (lower). **e** Binding energies of Cd atoms on the A (101), R (110), and A (101)-R (110) facets. **f** Correlative effects of N₂ calcination temperature, maximum interface density, and H₂ production rate (Inset shows the interface model). **g** HAADF-STEM images of 5Cd/P25 catalysts after H₂ pretreatment at 500 °C for 4 (left) and 8 (right) h. **h** Correlations among maximum interface density, H₂ production rate, and Cd loss rate following H₂ pretreatment.

resulting from the lattice mismatch between the A (101) and R (110) facets, leading to the formation of abundant Ti defects at the incoherent phase interface (asymmetric structure). Additionally, low-temperature EPR using 2, 4, 6-trichlorophenol as a hole scavenger detected a pronounced signal of electrons trapped in distorted Ti^{4+} tetrahedral sites at the P25 phase interface ($g = 1.979$) (Fig. 3c)[27]. However, the interface signal vanished upon the introduction of Cd, leaving only the signals from electrons trapped within the A lattice ($g_\perp = 1.982$) and surface ($g_\parallel = 1.922$). This observation suggests that the presence of distorted interface Ti^{4+} tetrahedral sites enhances electron transfer, thereby promoting the selective formation and stabilization of Cd single atoms at the phase interface. DFT calculations showed that the A (101) and R (110) facets could form a stable phase junction (Fig. 3d). The presence of a disordered interface and defects resulted in elevated surface energy (Supplementary Fig. 32). Consequently, Cd atoms were more readily anchored at the interface due to their substantially lower binding energy of −6.34 eV (Fig. 3e). This value was significantly more favorable compared to the binding energies observed for Cd atoms on the individual A (101) facet at −4.62 eV and the R (110) facet at −5.94 eV. These findings provided a plausible explanation for the preferential anchoring of Cd atoms at the phase interface in P25.

Notably, other active metals (e.g., Pt, Pd, Cu) deposited on P25 at equivalent concentrations (5 wt%) exhibited nanoparticle aggregation on its surface (Supplementary Fig. 33). However, single-atom formation of transition metals (e.g., Pt) on the P25 phase interface remained unattainable even at 0.2 wt% loading, concomitant with a marked decline in catalytic performance (Supplementary Fig. 34). These findings suggest that the formation of single atoms at the interface necessitates a favorable match between the metal's properties and the interfacial energy. The ionic radius of Cd differs more markedly from that of Ti than those of Pd, Pt, and Cu. Moreover, the electronegativity of Cd is most analogous to that of Ti (Supplementary Table 7). These characteristics may endow Cd atoms with a significant difference in average internal energy between the lattice and phase interface, rendering them particularly prone to segregation and anchoring at Ti defect sites within the interface, thereby minimizing the interfacial energy. This attribute elucidates the challenge faced by other metals in achieving single-atom dispersion at the P25 interface. Additionally, Cd single atoms at the phase interface were not observed when Cd was supported on a uniform mixture of 80% anatase and 20% rutile (5Cd/80A-20R), which exhibited reduced CH_3OH conversion (27.1%) and CO selectivity (3.7%) (Supplementary Fig. 35). This outcome implies that the unique phase interface structure of P25, enriched with defects, likely arises from an in situ phase transformation from anatase to rutile, where rutile nucleates and epitaxially grows on the anatase surface[28]. To validate this hypothesis, we systematically investigated the phase transformation by calcining A under static-air conditions at varying temperatures (Supplementary Fig. 36 and Supplementary Table 8). At a calcination temperature of 700 °C, the A/R weight fraction ratio of 80.2/19.8% and corresponding catalytic performance closely mirrored those of 5Cd/P25. HAADF-STEM images revealed the formation of Cd single atoms at the phase interface, which corroborated the formation of Ti defects through the in situ phase transformation.

We further investigated the effect of phase interface density on the catalytic performance. Employing a simplified geometric model that treated A and R particles as stacked cubes of distinct sizes, we calculated theoretical interface densities based on phase weight fractions and crystallite sizes (Supplementary Fig. 37 and Supplementary Table 8)[18]. Although calcining A in air-regulated phase weight fractions, the resulting interfacial density was limited to 4.7 $m^2 g^{-1}$ due to the enlarged crystallite size, which was lower than that of 5Cd/P25 (7.9 $m^2 g^{-1}$). Consequently, we implemented N_2 pretreatment (500–700 °C) on P25 to enhance interface density prior to Cd loading.

Increasing calcination temperature from 500 to 700 °C concurrently elevated the rutile weight fraction and crystallite size. Both maximum interface density and H_2 production rate followed volcano trends, peaking at 8.5 $m^2 g^{-1}$ and 266.0 mmol $g_{cat}^{-1} h^{-1}$, respectively, at 600 °C (Fig. 3f). Further interface engineering on P25 via H_2 pretreatment (500 °C, variable durations) adjusted phase ratios without substantially altering the crystallite size (Supplementary Table 8). Prolonged pretreatment was found to increase the interface density. Notably, the phase interface region appeared brighter after a 4-h H_2 pretreatment, and the number of bright interface bands significantly increased in the HAADF-STEM images (Fig. 3g left and Supplementary Fig. 38). Atomic-resolution analysis further revealed that the distinct bright interface bands correspond to dispersed Cd single atoms (Supplementary Fig. 38). Moreover, ICP-OES results showed that the Cd loss rate of the spent catalysts substantially decreased with the increase of the interface density (Fig. 3h). This trend suggests an increased number of single atoms stably anchored at the interface, thereby leading to a higher interface site density. A 4-h H_2 pretreatment yielded the highest interface density (10.1 $m^2 g^{-1}$) and a remarkable H_2 production rate of 292.9 mmol $g_{cat}^{-1} h^{-1}$ (Fig. 3h), exceeding conventional MSR catalysts (Supplementary Table 9). An 8-h pretreatment, however, resulted in the formation of small Cd particles (1–2.5 nm) (Fig. 3g right), which led to increased Cd loss after the reaction and compromised catalytic performance. This was likely attributed to the disruption of the phase interface structure.

Reaction mechanism studies

Since the reaction mechanism determines the product selectivity, we scrutinized various proposed reaction mechanisms for the novel catalysts, including methanol decomposition-water gas shift (MD − WGS), methyl formate hydrolysis, and formate decomposition (Supplementary Fig. 39). The MD reaction was initially investigated over the 5Cd/P25 catalyst at 290 °C under a methanol partial pressure of 20 kPa with a feed rate of 12 mL $g^{-1} h^{-1}$. CH_3OH conversion was limited to 1.7%, with CO_2 constituting ~77% of the products, accompanied by CO (~10%) and CH_4 (~13%) (Supplementary Fig. 40). The formation of CO_2 was proposed to originate from reactions between transient intermediates and hydroxyl groups (OH) on the catalyst support. Progressive depletion of surface OH species and accumulation of adsorbed intermediates correlated with the observed decline in methanol conversion to <1.0% over time. This finding indicates that, although thermodynamically favorable at high temperatures, MD is kinetically disfavored. Furthermore, comparative evaluation of WGS activity under equivalent conditions (290 °C, CO/H_2O = 1/1, P_{H_2O} = 20 kPa) revealed limited catalytic performance, with CO conversion decaying from 9.0% to 4.5% over 10 h and a correspondingly low H_2 production rate of 1.6 mmol $g^{-1} h^{-1}$. Strikingly, MSR under identical CH_3OH and H_2O partial pressures (20 kPa each) demonstrated a two-order-of-magnitude enhancement in H_2 production rates (264.7 mmol $g^{-1} h^{-1}$). These findings suggest that WGS contributes negligibly to H_2 generation, confirming that the MD-WGS pathway is unlikely to be viable for the Cd-based catalysts.

In situ diffuse reflectance infrared Fourier transform spectroscopy (DRIFTS) was conducted to elucidate the reaction mechanism. When exposed to CH_3OH/H_2O between 50 and 320 °C, only weak methanol physisorbed peaks (υ (CO) at 1000–1100 cm^{-1}, δ (CH) at 1300–1500 cm^{-1}, and υ (CH) at 2800–3000 cm^{-1}) were observed on A, R, and P25, aside from H_2O adsorption and *OH peaks (δ (H_2O) at 1651 cm^{-1} and υ (OH) at 3710 cm^{-1}) (Supplementary Fig. 41 and Supplementary Table 10). These findings demonstrate that the functionality of supports is limited to facilitating H_2O adsorption and dissociation. In stark contrast, after loading Cd single atoms, distinct methoxy (*CH_3O, δ (CH) at 1431 cm^{-1}) and bidentate formate (b-*$HCOO^-$, $υ_s$ (OCO) at 1336 cm^{-1}, $υ_{as}$ (OCO) at 1554 cm^{-1}) species emerged[5,29], which indicated that Cd single atoms were responsible for CH_3OH adsorption and dissociation (Fig. 4a–c). As the reaction
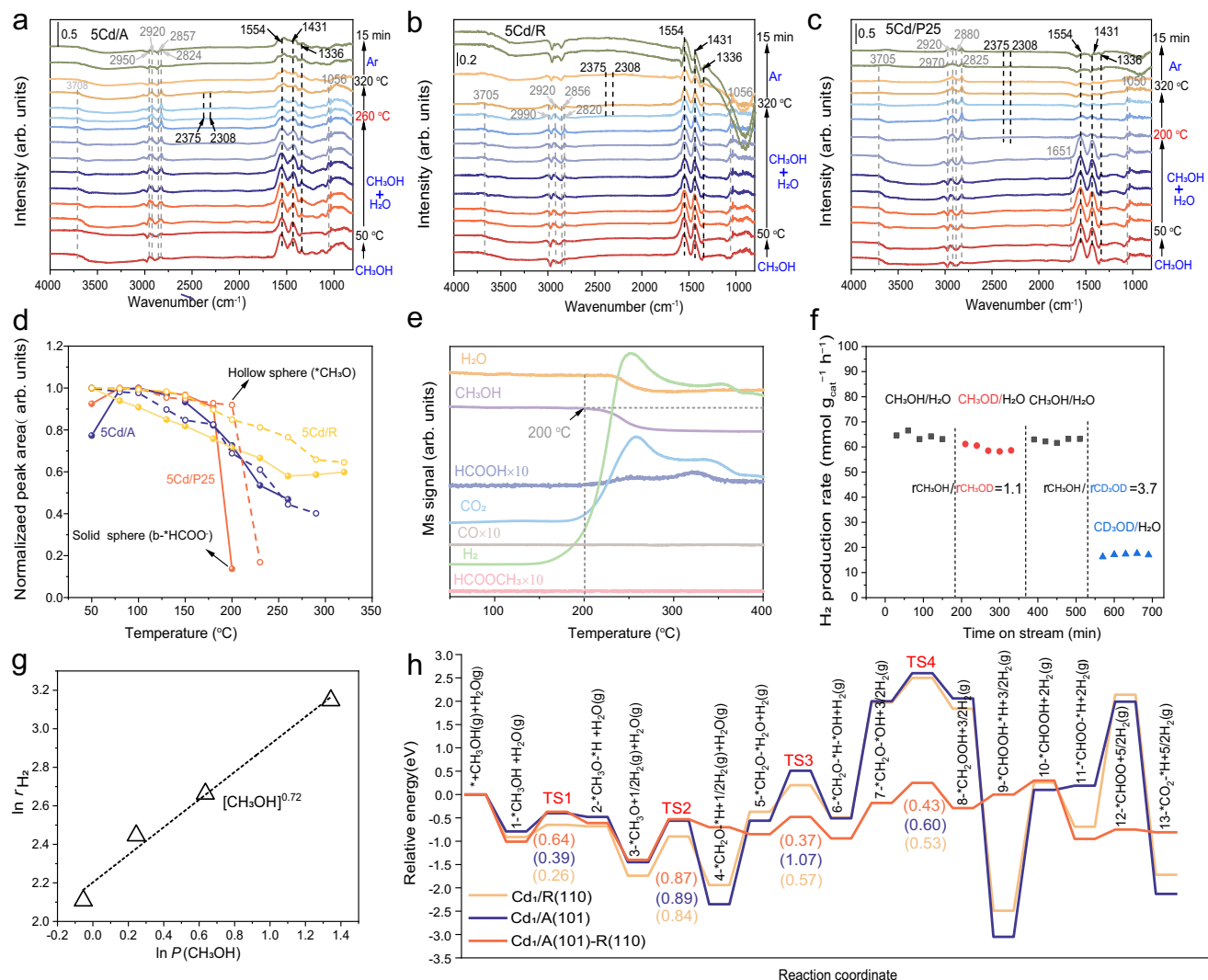
Fig. 4 | Elucidation of the reaction mechanism for Cd-based catalysts. a–c In situ DRIFTS spectra of MSR on 5Cd/A, 5Cd/R, and 5Cd/P25 at 50–320 °C. **d** Temperature-dependent changes in the normalized peak area of the *CH₃O (1431 cm⁻¹) and b-*HCOO⁻ (1554 cm⁻¹) species. **e** TPSR profiles for the 5Cd/P25

catalyst. **f** KIE measurements on the 5 Cd/P25 catalyst by modulating the isotopic composition of the feed gas. **g** Reaction order of CH_3OH on the 5 Cd/P25 catalyst. **h** Relative energy diagram depicting the formate decomposition pathway across three structural models.

temperature increased, the *CH₃O and b-*HCOO⁻ were rapidly consumed, coinciding with the emergence of gaseous CO_2 peaks at 2308 and 2375 cm⁻¹, indicating that H_2 generation resulted from formate transformation. Notably, on 5Cd/P25, *CH₃O and b-*HCOO⁻ were transformed more rapidly at a lower temperature (200 °C) compared to 5Cd/A (260 °C) and 5Cd/R (320 °C) (Fig. 4d). This trend aligns with the catalytic performance, implying that interfacial Cd single atoms are more conducive to intermediates transformation. Additionally, no characteristic peaks indicative of methyl formate (*HCOOCH₃) were detected in the 1700–1800 cm⁻¹ range during the reaction and the Ar sweeping stage[30]. Similarly, temperature-programmed surface reaction (TPSR) analyses exclusively identified formate species, with no indication of HCOOCH₃ (Fig. 4e and Supplementary Fig. 42). These findings rule out mechanism pathways involving methyl formate hydrolysis via esterification of formic acid with methanol, followed by its hydrolysis to yield CO_2 and H_2. Therefore, we propose that the formate decomposition pathway dominates the reaction mechanism on the SACs, where methanol initially decomposes into *CH₃O, subsequently dehydrogenates to *H₂CO, and reacts with *OH groups from dissociated H_2O to form *HCOO⁻. This intermediate then further dehydrogenates, yielding H_2 and CO_2.

The kinetic isotope effect (KIE) experiments were conducted on the 5Cd/P25 catalyst to reveal the reaction kinetics. Switching the feedstock from CH_3OH/H_2O to CH_3OD/H_2O resulted in essentially unchanged H_2 generation rates, yielding a KIE value (K_H/K_D) of 1.1 (Fig. 4f). In contrast, substituting CH_3OH/H_2O with CD_3OD/H_2O caused a dramatic 4-fold decline in H_2 production rates, corresponding to a significantly elevated KIE of 3.7. These findings establish that C−H bond cleavage exhibits substantially greater kinetic resistance than O−H bond scission, potentially identifying the rate-determining step (RDS) in the MSR reaction. To identify the specific RDS in elementary reactions, we derived the reaction rate equation based on the established formate mechanism. According to previous reports, assuming that methoxy dehydrogenation (*CH₃O→*CH₂O + *H) was RDS, the derived rate equation showed a first-order dependence on CH_3OH pressures (Supplementary Fig. 43). Considering competitive adsorption between CH_3OH and H_2O on active sites, the theoretical CH_3OH reaction order was predicted to be less than unity (<1). The experimentally determined CH_3OH reaction order of 0.72 demonstrated excellent agreement with the kinetic model (Fig. 4g), providing conclusive evidence that methoxy dehydrogenation constitutes the RDS in this pathway.

DFT calculations based on the established Cd_1/A (101), Cd_1/R (110), and Cd_1/A (101)-R (110) models provided complementary theoretical insights into the MSR reaction pathway. The computed energy landscape revealed distinct adsorption energy profiles: *CHO exhibited significantly lower adsorption energies on Cd_1/A (101) (−1.45 eV) and Cd_1/R (110) (−1.18 eV) compared to the Cd_1/A (101)-R (110) model (4.1 eV) (Supplementary Fig. 44). This energy disparity implies preferential CO generation pathways on Cd_1/A (101) and $Cd_1/$R (110) surfaces. Conversely, critical intermediates such as *CH_2O-*OH, *CHOOH, and *CHOO displayed substantially reduced adsorption energies on the Cd_1/A (101)-R (110) surface. These findings demonstrate that the formate decomposition pathway is thermodynamically more favorable on the Cd_1/A (101)-R (110) catalyst, attributable to its asymmetric coordination environment and enhanced charge density at the interface Cd single-atom sites.

The transition states of the formate decomposition pathway were further investigated (Fig. 4h and Supplementary Figs. 45–47). Consistent with in situ DRIFTS observations, DFT calculations revealed that both the adsorption and the stepwise dehydrogenation of CH_3OH occurred at the Cd active site. The activation energy barriers for CH_3OH dehydrogenation (TS1: 0.64 eV) were significantly lower than those for *CH_3O dehydrogenation (TS2: 0.87 eV) on the Cd_1/A (101)-R (110) surface. This clearly demonstrates that the C−H bond cleavage encounters higher kinetic resistance than O−H bond scission, aligning with the experimental KIE results. Following *CH_3O dehydrogenation to *CH_2O, H_2O adsorption and dissociation on adjacent Ti atoms generated *H and *OH species (TS3: 0.37 eV). Subsequent CH_2O/OH recombination formed CH_2OOH (TS4: 0.43 eV), which further dehydrogenated to produce CO_2 and H_2. Although TS1 and TS2 barriers on Cd_1/A (101)-R (110) were modestly elevated relative to Cd_1/A (101) (TS3/TS4: 1.07/0.60 eV) and Cd_1/R (110) (TS3/TS4: 0.57/0.53 eV), the dissociation of H_2O (TS3) and CH_2OOH formation (TS4) exhibited significantly lower energy barriers in the phase interface model. These results demonstrated that the unique structural properties of the interfacial structure enhanced the dissociation and activation of H_2O, thereby facilitating the subsequent formation of formate and H_2. Consequently, these observations rationalized the high activity and low CO selectivity of the 5Cd/P25 catalyst. Additionally, the highest activation energy barrier (TS2: 0.87 eV) confirmed *CH_3O dehydrogenation as the RDS on the Cd_1/A (101)-R (110), consistent with previous kinetic analysis.

3D printing of 5Cd/P25 for process optimization

Monolithic catalysts, renowned for their efficacy in enhancing heat and mass transfer and in reducing reaction pressures, were fabricated via direct-write 3D printing of 5Cd/P25 powder into structures with controlled pore dimensions (Fig. 5a). This method enabled kilogram-scale production while preserving structural integrity and mechanical robustness (Supplementary Fig. 48). Catalysts with reactor-optimized dimensions (Φ10 × 5 mm, Supplementary Fig. 49) showed peak performance at 0.5 mm pore size, achieving 100% CO_2 conversion over 100 h while suppressing CO concentration (0.07 mol%) and selectivity (0.3%) versus powder catalysts (Fig. 5b, Supplementary Fig. 50).

Post-reaction characterization confirmed the structural stability of the catalyst, with no signs of degradation or particle agglomeration (Supplementary Fig. 51). Computational Fluid Dynamics (CFD) simulations revealed that the monolithic catalyst featuring 0.5 mm pores possessed more compact linear channels, enhancing mass transfer while minimizing pressure drop to 0.0075 Pa (Fig. 5c and Supplementary Fig. 52). Additionally, smaller pores ensured a more uniform temperature profile and superior heat transfer. Consequently, these monolithic catalysts are poised to optimize industrial process performance.

Discussion

In summary, we have successfully anchored Cd single atoms at the phase interface of P25, a process driven by the compatibility of Cd atom properties and interface energy and the presence of abundant Ti defects. The resultant unique Cd-O−Ti interface sites, featuring asymmetric coordination geometry and elevated charge density, enable enhanced adsorption of reactants/intermediates. These structural attributes further reduce the energy barrier for both water dissociation and its activation within the formate decomposition pathway, thereby achieving complete methanol conversion with suppressed CO selectivity. The interface site density can be flexibly modulated to further boost catalytic activity. Moreover, the catalyst powders can be upscaled to monolithic forms via 3D printing, thereby improving mass and heat transfer characteristics. This research provides insights into the design of novel SACs and the development of practical MSR catalysts.

Methods
Chemicals

All chemicals were of analytical grade and were used as purchased without further purification. Cadmium nitrate tetrahydrate
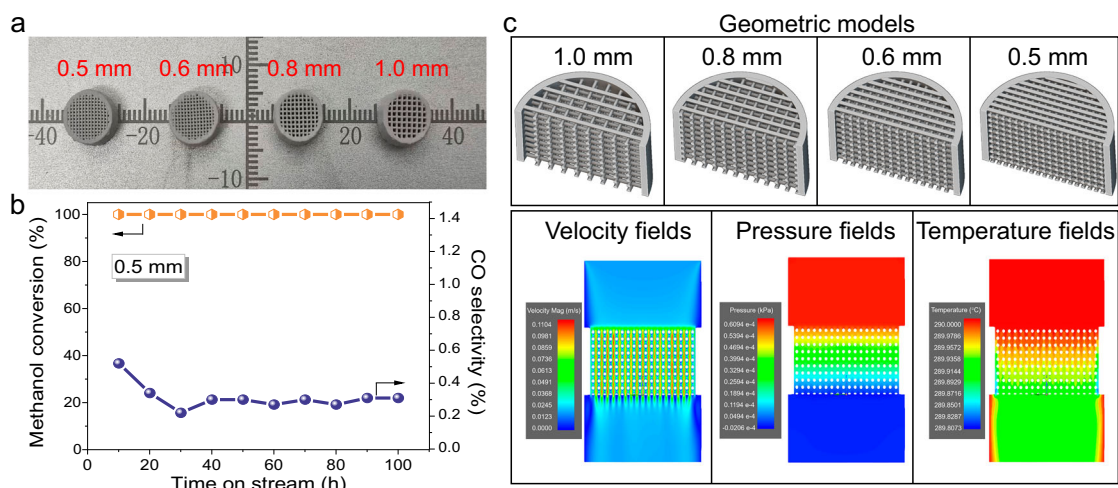

Fig. 5 | 3D printing and process simulation of the 5Cd/P25 catalyst. a 3D printing fabrication of monolithic 5Cd/P25 catalysts with tunable pore sizes (0.5–1.0 mm). **b** Catalytic performance assessment of the monolithic 5Cd/P25 catalyst with 0.5 mm pore size. **c** Multiphysics simulation of reaction-diffusion processes in the monolithic catalyst (0.5 mm pore size): velocity, pressure, and temperature fields.

(Cd(NO$_3$)$_2$·4H$_2$O), cupric nitrate trihydrate (Cu(NO$_3$)$_2$·3H$_2$O), chloroplatinic acid hexahydrate (H$_3$PtOCl$_6$), palladium nitrate (Pd(NO$_3$)$_2$·2H$_2$O) were purchased from Sinopharm Chemical Reagent Co. Degussa P25 was purchased from Evonik industries. Anatase, rutile, SiO$_2$, ZrO$_2$, ZnO, CeO$_2$, Al$_2$O$_3$, and 2, 4, 6-trichlorophenol were purchased from Aladdin Chemical Reagent Company. Bentonite was purchased from Shanghai Haohong Biopharmaceutical Technology Co. Hypromellose and polyvinyl alcohol 1799 were purchased from Shanghai Titan Scientific Co. Deionized water was used throughout this study.

Synthesis of supported Cd-based catalysts
All supported catalysts were synthesized via vacuum rotary impregnation. For instance, 5Cd/P25 was prepared by dispersing 1 g of Degussa P25 in 80 mL of deionized water, followed by the addition of 0.02 mmol mL^{-1} Cd(NO$_3$)$_2$·4H$_2$O (the loadings are equivalent to the metal-to-support mass ratio). The mixture was stirred for 1 h and then dried at 60 °C for 1 h using a vacuum rotary evaporator. The product was subsequently calcined at 500 °C for 3 h in static air. A similar method was employed for the synthesis of other supported Cd-based catalysts.

Synthesis of the 5Cd/80A-20R catalyst
A similar method was employed for the synthesis of the 5Cd/80A-20R catalyst, which involved combining 0.8 g of anatase and 0.2 g of rutile in 80 mL of deionized water, with the subsequent addition of 0.02 mmol mL^{-1} Cd(NO$_3$)$_2$·4H$_2$O, followed by stirring, drying, and calcination under identical conditions.

Synthesis of CdTiO$_3$
Cd(NO$_3$)$_2$·4H$_2$O (0.617 g) and P25 powder (0.160 g) were homogenously mixed through a rotary evaporation process at 65 °C. The mixture was then dried at 80 °C for 12 h and ground thoroughly with an agate mortar. The resulting samples were calcined at 650 °C for 8 h under static air, then immersed in 200 mL of 1 mol L^{-1} HNO$_3$ aqueous solution and stirred magnetically for 3 h. Solid-liquid separation was achieved through six cycles of centrifugation (4447 × g, 10 min each) with deionized water washing. The purified precipitate was dried at 80 °C for 12 h to obtain phase-pure CdTiO$_3$ powder.

Synthesis of CdTiO$_3$/TiO$_2$
1 g of rutile was dispersed in 80 mL of deionized water, followed by the addition of 0.08 mmol mL^{-1} Cd(NO$_3$)$_2$·4H$_2$O. The mixture was stirred for 12 h and then dried at 60 °C for 1 h using a vacuum rotary evaporator. The product was subsequently calcined at 700 °C for 3 h in static air.

Modulating phase interface and site densities through gaseous pretreatments
For air pretreatment, anatase was calcined in static air at temperatures of 600, 700, and 800 °C for 2 h each. For the N$_2$ pretreatment, P25 was calcined in a N$_2$ flow (100 mL min^{-1}) at temperatures of 500, 600, and 700 °C for 2 h each. Following this, the Cd precursor was deposited onto the pretreated P25 via vacuum rotary impregnation. For the H$_2$ pretreatment, P25 was reduced in a H$_2$ flow (100 mL min^{-1}) at 500 °C for durations of 2, 4, and 8 h. The Cd precursor was then similarly impregnated onto the P25. All pretreated samples were subsequently calcined at 500 °C for 3 h in static air.

3D printing
Initially, a homogeneous powder mixture was prepared by blending 90 wt% of our in-house synthesized 5Cd/P25, 5 wt% Bentonite, 3.5 wt% Hypromellos, and 1.5 wt% Poly (Vinyl Alcohol) (PVA) 1799 to a total of 100 g in an agate mortar. This powder mixture was then loaded into a 250 mL ball mill jar, to which a measured amount of deionized water and a small quantity of glycerin were added. Subsequently, the jar was placed into a planetary ball mill and stirred under settings of 580 rpm min^{-1}, with bidirectional milling for a duration of 15 h. The milling process culminated in a uniformly mixed printing slurry with appropriate rheological properties.

The rheological characterization of the 3D-printable 5Cd/P25 slurry, conducted using a HAAKE MARS 40 rheometer, revealed rapid viscosity recovery at both low and high shear rates, meeting the requirements for additive manufacturing processes.

The slurry formulated for 3D printing was loaded into a 50 mL syringe equipped with a 0.26 mm diameter print nozzle. Utilizing a Bio-Architect®WS 3D bioprinter, the printing parameters were set as follows: layer height of 0.17 mm, air pressure of 0.35 MPa, and a print speed of 10 mm s^{-1}. The cylindrical model specifications were a diameter of 9.2 mm and a height of 5 mm. By adjusting the printing gap, monolithic 5Cd/P25 catalysts with distinct pore sizes of 0.5 mm, 0.6 mm, 0.8 mm, and 1.0 mm were printed. These catalysts with varying pore sizes were subjected to freeze-drying for 24 h, followed by calcination in air at a heating rate of 5 °C min^{-1}, and maintained at 450 °C for 3 h to remove the organic binders. Kilogram-scale printing is achieved through continuous feeding.

Characterization
Metal loadings were detected by ICP-OES analysis on a Perkin-Elmer Optima 8000 instrument. XRD patterns were collected on a Rigaku Ultima IV X-ray powder diffractometer utilizing Cu Kα radiation (λ = 1.54056 Å) at 40 kV and 40 mA. Raman spectra were recorded on a Thermo Fisher Scientific DXR 2xi equipped with an electron-multiplying charge-coupled device (EMCCD) detector and a 514 nm Ar ion laser. XPS and AES analyses were conducted on a Thermo Fisher Scientific ESCALAB 250Xi. Calibration of the C1s peak for all catalysts was set at 284.8 eV. XANES and EXAFS spectroscopy were collected on the beamline BL11B in SSRF. Samples were homogeneously coated onto adhesive tape and measured at the Cd K-edge under ambient conditions using a Si (111) double-crystal monochromator. Data analysis was performed using Athena software. TEM and HRTEM analyses were conducted on a JEOL-JEM 2011 microscope operating at 200 kV. HAADF-STEM, EDX mapping, and EELS images were acquired on a JEM-ARM300F instrument. Scanning electron microscopy (SEM) images were acquired on a Zeiss Supra 55 at a low accelerating voltage of 5 kV. Nitrogen adsorption measurements were performed on a TriStar II 3020 analyzer. 100 mg of the sample was degassed at 200 °C under vacuum for 10 h, followed by nitrogen adsorption-desorption isotherms at 77 K. The specific surface area was determined using the Brunauer–Emmett–Teller (BET) equation, while the total pore volume and average pore size were assessed via the Barrett–Joyner–Halenda (BJH) method.

H$_2$-TPR analyses were conducted on a Micromeritics Autochem II 2920 instrument, integrated with a thermal conductivity detector (TCD) and an MKS Cirrus 2 mass spectrometer. For each measurement, 100 mg of the sample was initially purged with Ar at a flow rate of 30 mL min^{-1} and heated to 200 °C for 2 h to eliminate moisture, followed by cooling to 50 °C. The gas stream was then switched to H$_2$, and the temperature was ramped to 800 °C at a rate of 10 °C min^{-1}. CH$_3$OH-TPD measurements were executed using the same setup. After moisture removal and cooling to 50 °C, CH$_3$OH was absorbed onto the sample by Ar bubbling for 1 h. Excess surface adsorption was removed by Ar purging for 30 min until a stable baseline was achieved. The desorption process was then carried out from 50 to 500 °C. TPSR measurements followed a similar protocol, with a mixture of CH$_3$OH/H$_2$O (1/1) introduced by Ar bubbling as the temperature increased from 50 to 500 °C.

PALS was conducted using a high-resolution ORTEC fast-slow coincidence system, achieving a time resolution of approximately 201 ps. The samples were positioned symmetrically around a 5 mCi 22Na positron source, yielding a total count rate of 1 million counts.

CV measurements were conducted using an Autolab Electrochemical Workstation (PGSTAT302N) configured in a standard three-electrode setup. The fluorine-doped tin oxide (FTO) glass was cleaned ultrasonically with a mixture of acetone, ethanol, and water (1:1:1 v/v/v) for 30 min. The sample served as the working electrode, a platinum foil acted as the counter electrode, and a saturated Ag/AgCl electrode functioned as the reference electrode. For the preparation of the working electrode, 10 mg of the catalyst was mixed with 950 μL of a water/ethanol solution (1:1 v/v) and 50 μL of Nafion solution. After 30 min of sonication, 100 μL of the homogeneous suspension was applied to the cleaned FTO glass electrode with an active area of 2 cm × 1.5 cm and air-dried. The electrochemical cell was purged with argon to exclude oxygen interference. A 50 mL solution of 0.1 M H_2SO_4 served as the electrolyte, and the CV scans were performed at a scan rate of 20 mV s^{-1}.

In situ EPR spectra were acquired using a Bruker EMX Plus instrument. The presence of oxygen vacancies was detected within the field range of 3300–3500 G, corresponding to g-values from 1.94 to 2.04. Samples (0.1 g) were suspended in 100 g of a CH_3OH/H_2O (1/1) mixture. N_2 was flushed through the in situ cell to shield the samples from atmospheric interference. EPR signals were captured at both ambient and elevated temperatures (290 °C). For low-temperature EPR, spectra were recorded over the field range of 3200–3550 G with g-values spanning from 1.90 to 2.02 at a temperature of −213 °C. Powdered samples (0.2 g) were sonicated in 5 mL of ultrapure water, to which 5 mL of a 0.8 mM 2,4,6-trichlorophenol solution was added. The mixture was then deoxygenated by purging with N_2 for 1 h. A defined volume of this solution was cooled to −213 °C in the EPR in situ cell, where it was subjected to irradiation from a 300 W xenon lamp for 30 min. Following this, the EPR spectrum was recorded under constant light exposure and compared with a standard reference (g = 2.00285 ± 0.00005) to ensure the uniformity and precision of the g-tensor values.

Quasi-in situ XPS was performed on a Thermo Fisher Scientific ESCALAB 250Xi. Initially, samples were placed into the reaction chamber under a continuous flow of Ar (50 mL min^{-1}) and heated to 290 °C. Subsequently, the samples were transferred directly to the analysis chamber under vacuum to prevent air exposure for XPS analysis. Following analysis, the samples were returned to the reaction chamber, where they were exposed to a mixture of CH_3OH/H_2O, introduced via Ar bubbling for 2 h, prior to reanalysis in the XPS chamber. This procedure was also applied to samples that were subjected to a 4-h reaction, ensuring consistent methodology.

In situ DRIFTS measurements were performed on a Thermo FTIR spectrometer (Nicolet IS50) with a mercury-cadmium-telluride (MCT) detector. The in situ DRIFT spectra were recorded by collecting 64 scans at a resolution of 4 cm^{-1}. Prior to measurement, the sample was purged with Ar at 250 °C for 1 h to collect the background spectrum, and then cooled to 50 °C. The catalysts were exposed to CH_3OH and a CH_3OH/H_2O (1/1) mixture at a flow rate of 30 mL min^{-1} under atmospheric pressure. Spectra were recorded as the temperature and reaction time increased during the catalytic process.

Evaluation of catalytic performance

A continuous flow fixed-bed reactor (8 mm inner diameter) was used to evaluate catalytic performance. Typically, 0.2 g of catalyst (40–60 mesh) was packed between quartz wool plugs. After the reactor was increased to the set point, CH_3OH and H_2O were premixed in a specific molar ratio and pumped into the vaporizer operating at 180 °C with 1% N_2/Ar (30 mL min^{-1}) as both carrier gas and internal standard. Gaseous products were analyzed online using a Shimadzu GC-2014 C gas chromatograph equipped with a thermal conductivity detector (TCD) and a TDX-01 column for the analysis of H_2, N_2, CH_4, CO, and CO_2.

Methanol conversion and product selectivity were calculated as follows:

$$\text{Methanol conversion}\,(\%)$$
$$= \frac{n(\text{CO, outlet}) + n(\text{CO}_2, \text{outlet}) + n(\text{CH}_4, \text{outlet})}{n(\text{CH}_3\text{OH, inlet}) - n(\text{CH}_3\text{OH, outlet})} \times 100\% \quad (1)$$

$$\text{CO selectivity}\,(\%)$$
$$= \frac{n(\text{CO, outlet})}{n(\text{CO, outlet}) + n(\text{CO}_2, \text{outlet}) + n(\text{CH}_4, \text{outlet})} \times 100\% \quad (2)$$

$$\text{CO concentration}\,(\%)$$
$$= \frac{n(\text{CO, outlet})}{n(\text{H}_2, \text{outlet}) + n(\text{CO, outlet}) + n(\text{CO}_2, \text{outlet}) + n(\text{CH}_4, \text{outlet})} \times 100\% \quad (3)$$

$$\text{CO}_2 \text{ selectivity}\,(\%)$$
$$= \frac{n(\text{CO}_2, \text{outlet})}{n(\text{CO, outlet}) + n(\text{CO}_2, \text{outlet}) + n(\text{CH}_4, \text{outlet})} \times 100\% \quad (4)$$

$$\text{CH}_4 \text{ selectivity}\,(\%)$$
$$= \frac{n(\text{CO}_2, \text{outlet})}{n(\text{CO, outlet}) + n(\text{CO}_2, \text{outlet}) + n(\text{CH}_4, \text{outlet})} \times 100\% \quad (5)$$

$$\text{H}_2 \text{ production rate} = \frac{n(\text{H}_2, \text{outlet})}{m \times t} \quad (6)$$

where the n is the molar amount, m is the weight of catalysts, and t is the reaction time.

Computational details

The Vienna Ab initio Simulation Package (VASP) was used based on density functional theory (DFT)[31]. Using the electron exchange and correlation energy was treated within the generalized gradient approximation in the Perdew-Burke-Ernzerhof functional (GGA-PBE)[32]. The calculations were done with a plane-wave basis set defined by a kinetic energy cutoff of 400 eV. The energies were converged to 10^{-5} eV in the self-consistent field, and a conjugate-gradient algorithm was used to relax the atomic position until the forces acting on each atom were less than 0.02 eV Å^{-1}. The DFT-D$_3$ method developed by Grimme was applied in all calculations to describe the long-range dispersion interactions[33].

The GGA + U approach was used to treat the 3d orbital electrons of Ti with the effective Hubbard on-site Coulomb interaction parameter (U′ = U − J)[34]. The value of U′ was set to 4, according to the proposed value from previous works[35,36]. Bader charge analysis and charge density difference analyses were performed using VESTA to analyze the electron properties. The transition-state (TS) structures were searched using the climbing image nudged elastic band (CI-NEB) algorithm, with four images along the reaction pathway. All the minima and TS were confirmed through vibrational frequency calculations.

The anatase (101) slab models with 1 × 4 unit cells and rutile (110) models with 3 × 2 unit cells were cut from the optimized structures of bulk anatase (a = b = 3.870 Å and c = 9.563 Å) and bulk rutile (a = b = 4.695 Å and c = 3.071 Å). A vacuum layer of 15 Å was employed to prevent interactions between slabs. The lower-half layers of the slab were kept frozen, and the upper-half layers were allowed to relax. The k-point sampling was obtained from the Monkhorst-Pack scheme with a (2 × 3 × 1) mesh for optimization and electronic structure calculations. The heterostructures were constructed with rutile (110) and

anatase (101). One of the surface Ti atoms in the unit cell was substituted by a Cd atom, which served as the model for the catalysts.

The single-atom binding energy (E_B) is defined as the energy to introduce one Cd atom:

$$E_B = E_{tot}(Cd/TiO_2) - E_{tot}(Ti_{x-1}O_2) - E_{atom}(Cd) \qquad (7)$$

The vacancy formation energy (E_f) is defined as the defect formation energy of TiO_2 from the elimination of Ti atoms:

$$E_f = E_{tot}(Ti_{x-1}O_2) - E_{tot}(TiO_2) - (-\mu Ti) \qquad (8)$$

Computational fluid dynamics (CFD) simulation
To investigate the flow diffusion phenomena, pressure drop, and heat transfer effects of monolithic catalysts with varying porosities, CFD simulations were performed using the software OpenFOAM®−12 (OpenFOAM-12 owned, developed, and released by the OpenFOAM Foundation openfoam.org). A simplified geometric model of the monolithic catalyst was constructed using the software ZWSOFT®, closely resembling the actual dimensions and structure, with individual pillar diameters of 0.26 mm and spacings of 0.5 mm, 0.6 mm, 0.8 mm, and 1.0 mm for the 3D Cd/TiO_2 monolithic catalysts, corresponding to surface areas of 2149.7 mm^2, 1853.7 mm^2, 1489.8 mm^2, and 1255.9 mm^2, respectively. CH_3OH/H_2O was used as the flowing medium to simulate the flow (0.110 m s^{-1}, 0.085 m s^{-1}, 0.082 m s^{-1}, and 0.073 m s^{-1}) and temperature fields. The actual operation of structured catalysts is highly complex, involving the coupling of various physical and chemical processes, such as turbulence, heat transfer, mass transfer, and chemical reactions. Therefore, the actual process was simplified under the assumption that no chemical reactions occur as the gas flows through the structured catalyst, the gas at the entrance is in a steady flow state, and fully expands shortly after the entrance; the reactor wall temperature is kept constant. Under these assumptions, the flow and temperature fields of the structured catalyst were meticulously simulated, with intensive grid refinement at the catalyst site and repeated iterative processes after providing initial boundary conditions.

Estimation of Cd usage for a commercial PEMFC vehicle
The 2023 Toyota Mirai is reported to consume 1.4 kg of H_2 for every 100 miles and has a range of 300–400 miles (US Department of Energy. Compare Fuel Cell Vehicles http://www.fueleconomy.gov/feg/fcv_sbs.shtml). We estimate the amount of Cd/P25 catalyst required as follows: traveling at 100 miles per hour, the Mirai's hydrogen consumption rate is 1.4 kg per hour. With a hydrogen production rate of 268 mmol g$_{cat}^{-1}$ h^{-1} for the Cd/P25 catalyst, approximately 2.6 kg of this catalyst would be needed to meet the Mirai's hourly demand. This is only a theoretical estimate, and practical applications still need to solve engineering process problems and further optimize to meet the application.

Data availability
The authors declare that the data supporting the findings of this study are available within the paper and its supplementary information files. The DFT calculation data generated in this study have been deposited in Figshare (data https://doi.org/10.6084/m9.figshare.27905838)[37].

References
1. Palo, D. R., Dagle, R. A. & Holladay, J. D. Methanol steam reforming for hydrogen production. *Chem. Rev.* **107**, 3992–4021 (2007).
2. Sá, S., Silva, H., Brandão, L., Sousa, J. M. & Mendes, A. Catalysts for methanol steam reforming—A review. *Appl. Catal. B* **99**, 43–57 (2010).
3. Xu, X., Shuai, K. & Xu, B. Review on copper and palladium based catalysts for methanol steam reforming to produce hydrogen. *Catalysts* **7**, 183 (2017).
4. Sun, Z. & Sun, Z. Hydrogen generation from methanol reforming for fuel cell applications: a review. *J. Cent. South Univ.* **27**, 1074–1103 (2020).
5. Li, D. et al. Induced activation of the commercial Cu/ZnO/Al₂O₃ catalyst for the steam reforming of methanol. *Nat. Catal.* **5**, 99–108 (2022).
6. Kaiser, S. K., Chen, Z., Faust Akl, D., Mitchell, S. & Perez-Ramirez, J. Single-atom catalysts across the periodic table. *Chem. Rev.* **120**, 11703–11809 (2020).
7. Mitchell, S., Vorobyeva, E. & Pérez-Ramírez, J. The multifaceted reactivity of single-atom heterogeneous catalysts. *Angew. Chem. Int. Ed.* **57**, 15316–15329 (2018).
8. Pan, Y., Zhang, C., Liu, Z., Chen, C. & Li, Y. Structural regulation with atomic-level precision: from single-atomic site to diatomic and atomic interface catalysis. *Matter* **2**, 78–110 (2020).
9. Wang, A., Li, J. & Zhang, T. Heterogeneous single-atom catalysis. *Nat. Rev. Chem.* **2**, 65–81 (2018).
10. Huang, W. et al. Steam-created grain boundaries for methane C–H activation in palladium catalysts. *Science* **373**, 1518–1523 (2021).
11. Tang, C., Gong, P., Xiao, T. & Sun, Z. Direct electrosynthesis of 52% concentrated CO on silver's twin boundary. *Nat. Commun.* **12**, 2139 (2021).
12. Huang, Q. et al. Twinning-assisted dynamic adjustment of grain boundary mobility. *Nat. Commun.* **12**, 6695 (2021).
13. Kabiraz, M. K. et al. Understanding the grain boundary behavior of bimetallic platinum–cobalt alloy nanowires toward oxygen electroreduction. *ACS Catal.* **12**, 3516–3523 (2022).
14. Man, P., Srolovitz, D., Zhao, J. & Ly, T. H. Functional grain boundaries in two-dimensional transition-metal dichalcogenides. *Acc. Chem. Res.* **54**, 4191–4202 (2021).
15. Bai, S., Zhang, N., Gao, C. & Xiong, Y. Defect engineering in photocatalytic materials. *Nano Energy* **53**, 296–336 (2018).
16. Ruan, X. et al. Catalyzing artificial photosynthesis with TiO_2 heterostructures and hybrids: emerging trends in a classical yet contemporary photocatalyst. *Adv. Mater.* **36**, 2305285 (2024).
17. Ma, Y., Wang, X. & Li, C. Charge separation promoted by phase junctions in photocatalysts. *Chin. J. Catal.* **36**, 1519–1527 (2015).
18. Jiang, Y. et al. Elevating photooxidation of methane to formaldehyde via TiO_2 Crystal Phase Engineering. *J. Am. Chem. Soc.* **144**, 15977–15987 (2022).
19. Monai, M. et al. Restructuring of titanium oxide overlayers over nickel nanoparticles during catalysis. *Science* **380**, 644–651 (2023).
20. Hussain, H. et al. Structure of a model TiO_2 photocatalytic interface. *Nat. Mater.* **16**, 461–466 (2017).
21. Scanlon, D. O. et al. Band alignment of rutile and anatase TiO_2. *Nat. Mater.* **12**, 798–801 (2013).
22. Gao, C. et al. A photoresponsive rutile TiO_2 heterojunction with enhanced electron–hole separation for high-performance hydrogen evolution. *Adv. Mater.* **31**, 1806596 (2019).
23. Ruan, X. et al. Favorable energy band alignment of TiO_2 anatase/rutile heterophase homojunctions yields photocatalytic hydrogen evolution with quantum efficiency exceeding 45.6. *Adv. Energy Mater.* **12**, 2200298 (2022).
24. Zhou, H. et al. Facet-dependent electron transfer regulates photocatalytic valorization of biopolyols. *J. Am. Chem. Soc.* **144**, 21224–21231 (2022).
25. Zhang, D. et al. Regulating spin polarization through cationic vacancy defects in $Bi_4Ti_3O_{12}$ for enhanced molecular oxygen activation. *Angew. Chem. Int. Ed.* **62**, e202303807 (2023).
26. Pan, L. et al. Manipulating spin polarization of titanium dioxide for efficient photocatalysis. *Nat. Commun.* **11**, 418 (2020).

27. Li, G. et al. The important role of tetrahedral Ti^{4+} sites in the phase transformation and photocatalytic activity of TiO_2 nanocomposites. *J. Am. Chem. Soc.* **130**, 5402–5403 (2008).

28. Zhang, H. & Banfield, J. F. Polymorphic transformations and particle coarsening in nanocrystalline titania ceramic powders and membranes. *J. Phys. Chem. C* **111**, 6621–6629 (2007).

29. Zhang, S. et al. Morphological modulation of Co_2C by surface-adsorbed species for highly effective low-temperature CO_2 reduction. *ACS Catal.* **12**, 8544–8557 (2022).

30. Meng, H. et al. Designing Cu^0–Cu^+ dual sites for improved C–H bond fracture towards methanol steam reforming. *Nat. Commun.* **14**, 7980 (2023).

31. Kresse, G. & Furthmüller, J. Efficiency of ab-initio total energy calculations for metals and semiconductors using a plane-wave basis set. *Comput. Mater. Sci.* **6**, 15–50 (1996).

32. Perdew, J. P. et al. Atoms, molecules, solids, and surfaces: applications of the generalized gradient approximation for exchange and correlation. *Phys. Rev. B* **46**, 6671–6687 (1992).

33. Grimme, S., Antony, J., Ehrlich, S. & Krieg, H. A consistent and accurate ab initio parametrization of density functional dispersion correction (DFT-D) for the 94 elements H-Pu. *J. Chem. Phys.* **132**, 154104 (2010).

34. Dudarev, S. L., Botton, G. A., Savrasov, S. Y., Humphreys, C. J. & Sutton, A. P. Electron-energy-loss spectra and the structural stability of nickel oxide: an LSDA+U study. *Phys. Rev. B* **57**, 1505–1509 (1998).

35. Yin, X. et al. Diffusion versus desorption: complex behavior of H atoms on an oxide surface. *Chemphyschem* **9**, 253–256 (2008).

36. Islam, M. M., Calatayud, M. & Pacchioni, G. Hydrogen adsorption and diffusion on the anatase TiO_2 (101) surface: a first-principles investigation. *J. Phys. Chem. C* **115**, 6809–6814 (2011).

37. Zhang, S. et al. Phase-interface-anchored cadmium single-atom catalysts for efficient methanol steam reforming. *Figshare.* https://doi.org/10.6084/m9.figshare.27905838 (2025).

Acknowledgements

Author contributions

S.Z. and H.W. designed the project. H.W. and Y.S. guided and supervised the research. S.Z., H.Z., and Z.S. performed the catalyst preparation and catalytic reaction test. S.Z., Z.S., H. Liang, and R.Z. conducted the characterization. B.W. contributed to DFT calculations. Z.H. performed research on 3D printing. S.Z., X.L., H. Luo, L.X., and H.W. analyzed the data and wrote the paper. All authors contributed to the discussion of the results.

Competing interests

The authors declare no competing interests.

Additional information

Supplementary information The online version contains supplementary material available at https://doi.org/10.1038/s41467-025-63060-7.

Correspondence and requests for materials should be addressed to Hui Wang.

Peer review information *Nature Communications* thanks Navneet Kumar Gupta and the other anonymous reviewer(s) for their contribution to the peer review of this work. A peer review file is available.

Reprints and permissions information is available at http://www.nature.com/reprints

Publisher's note Springer Nature remains neutral with regard to jurisdictional claims in published maps and institutional affiliations.